Simulation of Red Blood Cell Migration in Small Arterioles: Effect of Cytoplasmic Viscosity

Amir Saadat[1], Christopher J. Guido[1], and Eric S. G. Shaqfeh[1,2,3,*]

[1] Department of Chemical Engineering, Stanford University, Stanford, CA 94305, USA
[2] Department of Mechanical Engineering, Stanford University, Stanford, CA 94305, USA
[3] Institute for Computational and Mathematical Engineering, Stanford University, Stanford, CA 94305, USA

Abstract

The dynamics of red blood cells in small arterioles are important as these dynamics affect many physiological processes such as hemostasis and thrombosis. However, studying red blood cell flows theoretically is challenging due to the complex shapes of red blood cells and the non-trivial viscosity contrast of a red blood cell. To date little progress has been made studying small arteriole flows (20-40μm) with a hematocrit (red blood cell volume fraction) of 10-20% and a physiological viscosity contrast. In this work, we present the results of large-scale simulations that show how the channel size, viscosity contrast of the red blood cells, and hematocrit effect cell distributions and the cell free layer in these systems. We utilize a massively-parallel immersed boundary code coupled to a finite volume solver to capture particle resolved physics in these systems. We show that channel size qualitatively changes how the cells distribute in the channel. Our results also indicate that at a hematocrit of 10% that the viscosity contrast is not negligible when calculating the cell free layer thickness. We explain this result by comparing lift and collision trajectories of cells at different viscosity contrasts.

Introduction

Microcirculation in vascular systems is a vital component of living organisms where oxygenated blood passes through terminal arterioles (smaller blood vessels with 20 – 50 micron diameter) and capillaries ($\sim$10 microns) (Fung, 1997; Secomb, 2017). Whole blood is a complex fluid composed of plasma as the suspending medium and three main cellular components: red blood cells (RBCs), platelets and white blood cells. Red blood cells take up to 45% volume fraction (Hematocrit) in the whole blood and are the oxygen carriers with biconcave shape with equivalent radius of about 2.82 μm. Their reduced volume is about 0.65 ($\nu = 3\sqrt{4\pi}\frac{V}{S^{3/2}}$, where V is the cell volume and S is its surface area) (Evans and Fung, 1972; Pozrikidis, 2003; Fischer et al., 1981). RBCs are highly flexible (Eggleton and Popel, 1998) due to their soft elastic properties and their relatively low reduced volume. This in turn causes the cells to migrate away from the vessel walls when they are exposed to the blood stream.

The migration of RBCs is of direct biological importance – as the cells move towards the centerline in pressure driven flows, a cell-free layer is formed near the vessel walls (also known as Fahraeus-Lindqvist layer) (Fåhræus and Lindqvist, 1931). This layer is known to contribute in the reduction of the blood viscosity or plasma skimming as blood perfuses the smaller vessels (Freund, 2014; Pries and Secomb, 2003). In addition, the migration of the red blood cells induces the margination of stiffer platelets by volume exclusion (Spann et al., 2016; Fitzgibbon et al., 2015; Reasor et al., 2013; Vahidkhah, 2015; Haga et al., 1998; Bächer et al., 2018). These marginated platelets are now better located to participate in reactions with the endothelial cells in the event of an injury when the clotting cascade begins (Mitrophanov et al., 2014; Govindarajan et al., 2016).

Individual cell migration is partly due to a wall-induced lift force, with the velocity proportional to the stresslet, i.e., the symmetric part of the first moment of particle surface traction and inversely proportional to the squared vertical distance from the walls (Smart and Leighton, 1991; Zhao et al., 2012). There is another lift mechanism in pressure driven flows, due to the non-zero curvature of the flow field which drives the cells closer to the center-line, in order to minimize particle deformation Coupier et al. (2008); Danker et al. (2009). It has been shown that the lift velocity generally depends on Ca, λ, and the height of the channel (Qi and Shaqfeh, 2017).

The shape and the mode of particle rotation, namely tank-treading, tumbling, swinging, or breathing motion (Bagchi and Kalluri, 2009; Yazdani, 2012; Fedosov et al., 2014), are correlated with the lift velocity. More symmetric shapes and tumbling motion are expected to reduce the lift velocity. For instance, at Ca $= 0.25$, an RBC is in the tumbling regime Sinha and Graham (2015) and therefore the migration is slower, whereas for Ca≥ 0.5, the RBC is in the tank-treading regime and lifts more quickly (Qi and Shaqfeh, 2017; Saadat et al., 2018). Slipper-like and parachute-like shapes for RBCs have been extensively reported in the literature Kaoui et al. (2009); Quint et al. (2017); Fedosov et al. (2014); Tomaiuolo et al. (2016); Guckenberger et al. (2018). However, experiments of Lanotte et. al (Lanotte et al., 2016) clearly revealed existence of more complicated multi-lobe shapes. Remarkably, there is a rich spectrum of shape states and motion that RBCs may undergo depending on the initial condition (Guckenberger et al., 2018), the ratio of convective forces to elastic restoring forces (denoted by the capillary number) (Sinha and Graham, 2015), and also the confinement level of the vessel (Reichel et al., 2018).

The collective behavior of a RBC suspension is more complicated than single cell dynamics. The RBC volume fraction is 45% in whole blood, however, the physiological hematocrit levels of the micro-circulation are much lower. This reduction occurs when the blood flows from the arteries to arterioles and capillaries. The hematocrit in small vessels may be 10% or lower due to this Zweifach-Fung effect (Fung, 1997; Shen et al., 2016; Pries and Secomb, 2003). At these volume fractions, it is crucial to capture the interaction of the cells to describe the overall collective dynamics of an RBC suspension (Pranay et al., 2012; Narsimhan et al., 2013; Qi and Shaqfeh, 2017, 2018). In fact, the average local hematocrit of RBCs (or cell concentration distribution ϕ) has a nontrivial form that is a strong function of the channel size and is a direct result of the interplay between the hydrodynamic lift and cellular interaction (Qi, 2017). Collision models have been developed over the last decade to approximate the form of the concentration distribution and a simple advection-diffusion equation with only binary diffusion can be successful in predicting these distributions for wide channels (Qi, 2017; Pranay et al., 2012).

Due to the complexity of blood suspension dynamics, large scale simulation tools are required to understand much of the salient physics. Many approaches have been developed including the boundary integral method (Zhao et al., 2012; Sinha and Graham, 2015; Pozrikidis, 1992), the immersed boundary method coupled with the Lattice Boltzmann method (Shen et al., 2016; Krüger, 2012; Reasor et al., 2013; Závodszky et al., 2017; de Haan et al., 2018), and other immersed boundary approaches coupled to finite volume/difference/element solvers (Ye et al., 2016; Doddi, 2008; Balogh and Bagchi, 2018; Sigüenza et al., 2016; Saadat et al., 2018). The boundary integral method (BEM) has had great success in simulating smaller suspensions of cells, but poor scaling in particle number often reduces the ability to study larger suspensions via BEM. Additionally, many authors report instabilities when studying large viscosity contrasts when studying suspensions. The Lattice Boltzmann method has shown extremely good scaling in particle number and also the ability to study important features like the viscosity contrast – the viscosity ratio of inner cell cytoplasm to the outer plasma – which makes it a promising simulation technique (Shen et al., 2016; de Haan et al., 2018). In a similar manner, immersed boundary methods coupled to finite volume solvers or finite element solvers have also shown great promise in simulating these large suspensions and we will be utilizing this method to further elucidate the physics of these suspensions (Saadat et al., 2018; Balogh and Bagchi, 2018). Our method utilizes a finite volume flow solver and finite elements to model the physics of the RBCs. This method scales well with particle number, can handle complex unstructured geometries, and can adequately resolve viscosity contrasts in the physiological range.

Viscosity contrast affects shape, mode of motion, and collision dynamics (Sinha and Graham, 2015;

Omori et al., 2014; Lanotte et al., 2016; de Haan et al., 2018; Ye et al., 2010; Freund and Orescanin, 2011; Zhao et al., 2010). A large body of simulations in the literature have been conducted with the viscosity ratio in the range of $\lambda \leq 3$ (Zhao et al., 2012; Qi and Shaqfeh, 2017; Narsimhan et al., 2013; Fedosov et al., 2010; Foessel et al., 2011), however, the physiological value is nearly 5 (Secomb, 2017; Lanotte et al., 2016). For boundary integral simulations, high viscosity ratio may result in an undesirable mode of rotation (Narsimhan et al., 2013), buckling Foessel et al. (2011) or a numerical instability Omori et al. (2013, 2014); Qi (2017). The literature regarding the conditions under which the viscosity ratio affects RBC suspension behavior is small and incomplete. 2D LB simulations of Shen et al. (2016) in a bifurcated channel suggested that there is a significant impact on the local RBC distribution of the parent channel when $\lambda = 10$ compared to no viscosity contrast. Recent LB simulations of de Haan et al. (2018) indicated increasing impact of the viscosity contrast for higher flow strength (Reynolds number). They performed the simulations for large channels (70 μm in diameter) and observed negligible importance of λ on cell-free-layer and also local hematocrit for Ht values down to 20%.

In this work, we present the results of large scale simulations of suspensions of red blood cells in the micro-circulation (channels with a size $\leq 50\mu$m). We investigate the role that channel size has on the RBC distribution and the time dependence of its evolution. Notably we observe that the distribution does not reach a steady state as has been previously reported in literature and actually continues to show fluctuations over long times. Additionally, we consider the effect of viscosity contrast (λ) on the cell distributions in these small channels at physiological hematocrit 10-20%. We report that in these smaller channels the viscosity contrast has a measurable impact on the CFL thickness if the concentration of RBCs is at the low end of the physiological range and explain these results based on the measured lift and binary collisions observed for single cells and cell pairs. Our results suggest that the parameters involved in simpler "Boltzmann collision" theories, namely, the collisional displacement and lift, need to be modified to take into account the higher viscosity contrast.

Materials and Methods

Governing Equations and Methodology

We consider the dynamic problem of an elastic RBC suspended in an incompressible Newtonian fluid, where the suspended RBC is neutrally buoyant. The total domain under consideration is defined to be Ω which will be broken into two sub-domains Ω^{f} and Ω^{m} which represent the volume of the fluid and the suspended RBC respectively (the m superscript given here to represent "membrane" as opposed to "fluid"). The governing equations are conservation of momentum in both the fluid and membrane sub-domains as well as continuity:

$$\rho \frac{\mathrm{D}\boldsymbol{v}}{\mathrm{D}t} = \nabla \cdot \boldsymbol{\sigma}^{\mathrm{f}} \quad \boldsymbol{x} \in \Omega^{\mathrm{f}}, \tag{1}$$

$$\rho \frac{\mathrm{D}\boldsymbol{v}}{\mathrm{D}t} = \nabla \cdot \boldsymbol{\sigma}^{\mathrm{m}} \quad \boldsymbol{x} \in \Omega^{\mathrm{m}}, \tag{2}$$

$$\nabla \cdot \boldsymbol{v} = 0 \quad \in \Omega. \tag{3}$$

We have defined the stress in the RBC and fluid to be $\boldsymbol{\sigma}^{\mathrm{m}}$ and $\boldsymbol{\sigma}^{\mathrm{f}}$ respectively. At the boundary of contact between the membrane and the liquid we also require a stress balance to be satisfied. We denote the boundary with an outwardly-pointing unit normal $\boldsymbol{n}$. We write the stress balance condition as

$$(\boldsymbol{\sigma}^{\mathrm{m}} - \boldsymbol{\sigma}^{\mathrm{f}}) \cdot \boldsymbol{n} = 0 \quad \boldsymbol{x} \in \Omega^{\mathrm{m}}. \tag{4}$$

We represent the suspending fluid stress as a Newtonian stress,

$$\boldsymbol{\sigma}^{\mathrm{f}} = \boldsymbol{\sigma}^{\mathrm{N}} = -p\mathbf{I} + \eta \left(\frac{\partial \boldsymbol{v}}{\partial \boldsymbol{x}} + \frac{\partial \boldsymbol{v}}{\partial \boldsymbol{x}}^{\mathrm{T}} \right). \tag{5}$$

In the above, we have defined p to be the hydrodynamic pressure and η to be the Newtonian fluid viscosity.

We also must specify a constitutive model for the RBCs. The RBC will be modeled as a 2D hyper-elastic membrane. The second Piola-Kirchhoff tension, $\hat{\mathbf{S}}$, is calculated using the principle of virtual work from the strain energy areal density $\hat{W}$, which is a function of the invariants of the right Cauchy-Green tensor $\hat{\mathbf{C}} = \hat{\mathbf{F}}^{\mathrm{T}}\hat{\mathbf{F}}$. $I_1^{\hat{C}}$ and $I_2^{\hat{C}}$ are the two independent invariants of $\hat{\mathbf{C}}$ in this reduced system and the following relationship is utilized to calculate stress:

$$\hat{\mathbf{S}} = 2\frac{\partial \hat{W}}{\partial \hat{\mathbf{C}}} = 2\left\{\frac{\partial \hat{W}}{\partial I_1^{\hat{C}}}\mathbf{I} + J^2\hat{\mathbf{C}}^{-1}\frac{\partial \hat{W}}{\partial I_2^{\hat{C}}}\right\}. \tag{6}$$

The well -known Skalak model is used for the energy areal density:

$$\hat{W} = \frac{\hat{\mu}_p}{2}\left(\frac{1}{2}I_1^2 + I_1 - I_2\right) + \frac{\hat{\mu}_D}{8}I_2^2. \tag{7}$$

where $I_1 = I_1^{\hat{C}} - 2$ and $I_2 = I_2^{\hat{C}} - 1$ are the two invariants of the Skalak model. The Skalak model is generally used to enforce local area-incompressibility in a membrane so the dilatational modulus, $\hat{\mu}_D$, is set to be much larger than the shear modulus, $\hat{\mu}_p$.

Since we have neglected the out of plane forces in the membrane approximation, we also include the bending energy in our model. This provides an additional energy density function for bending:

$$\hat{W}_B = \frac{k_B}{2}\left(2\kappa_H + c_0\right)^2. \tag{8}$$

In the above expression we have defined k_b as the bending modulus, c_0 as the spontaneous curvature of the membrane, and κ_H as the mean curvature of the membrane.

Numerical Implementation

To solve the coupled fluid-solid problem we utilize an Immersed Finite Element Method (IFEM). More details about this method can be found in a recent publication (Saadat et al., 2018). To arrive at the governing equations, we rewrite Eqns. 1 and 2 as a single equation over the total domain as follows:

$$\rho\frac{\mathrm{D}\boldsymbol{v}}{\mathrm{D}t} = \nabla\cdot\boldsymbol{\sigma}^{\mathrm{f}} + \boldsymbol{f}^{\mathrm{IB}} \quad \boldsymbol{x}\in\Omega, \tag{9}$$

where $\boldsymbol{f}^{\mathrm{IB}}$ is the immersed boundary force density. It is clear that for conservation of momentum to be satisfied everywhere, the immersed boundary force density must take the following form:

$$\boldsymbol{f}^{\mathrm{IB}} = \nabla\cdot(\boldsymbol{\sigma}^{\mathrm{m}} - \boldsymbol{\sigma}^{\mathrm{f}}) \quad \boldsymbol{x}\in\Omega^{\mathrm{m}}. \tag{10}$$

The discretized immersed boundary method utilizes two separate grids. The Lagrangian grid (Ω^{m}) while a second fixed Eulerian grid is utilized for the entire domain ($\Omega^{\mathrm{m}} + \Omega^{\mathrm{f}} = \Omega$).

We distinguish between the immersed boundary force on the Lagrangian grid and the immersed boundary force in the Eulerian domain which are defined to be $\boldsymbol{F}^{\mathrm{IB,m}}$ and $\boldsymbol{F}^{\mathrm{IB,f}}$ respectively (note that force densities are given by a lowercase $\boldsymbol{f}$ and forces are given by uppercase $\boldsymbol{F}$).

On the Eulerian domain we therefore solve the following expression with a third order accurate finite volume scheme developed at Stanford's Center for Turbulence research (Ham et al., 2006):

$$\rho\frac{\mathrm{D}\boldsymbol{v}}{\mathrm{D}t} = \nabla\cdot\boldsymbol{\sigma}^{\mathrm{f}} + \boldsymbol{f}^{\mathrm{IB,f}} \quad \boldsymbol{x}\in\Omega. \tag{11}$$

We are left to determine the values of $\boldsymbol{F}^{\mathrm{IB,m}}$ for which we utilize finite elements. Details of this expression can be found in a more detailed computational methods paper published elsewhere (Saadat et al., 2018).

Membrane immersed boundary models have additional special considerations. The viscosity of the fluid inside the membrane may not be the same as the exterior fluid. The second important consideration is that the volume of the capsule can drift over time due to interpolation errors, necessitating explicit correction.

For the simulation of RBCs, we solve the following Poisson equation to determine which nodes of the fluid domain are inside the membrane boundaries (this information is encoded as an indicator function I):

$$\nabla^2 I = \nabla \cdot \mathbf{G}, \tag{12}$$

where

$$\mathbf{G} = \int_{\Omega^{\mathrm{m}}} \mathbf{n} \mathrm{d}S.$$

For details of this implementation see Bagchi and Kalluri (2009).

Using this information, the RBC internal fluid can be assigned variable viscosity ratios. We can subsequently set the viscosity in the fluid domain to be:

$$\eta_0 = \eta_{\mathrm{out}} + (\eta_{\mathrm{in}} - \eta_{\mathrm{out}})I.$$

Additionally, since the divergence free character of the flow is not preserved exactly during the velocity interpolation step in the immersed boundary method, the RBCs modeled using a thin membrane may undergo a gradual volume change during the simulation (Note that even though the relative volume change is typically on the order of 10^{-4} and smaller in a single time step, the associated numerical error will propagate and will cause errors of a few percent by the end of the simulation). In order to avoid this, we exploit the volume conservation algorithm proposed by Mendez et al. (2014).

Non-dimensional Equations

We can write all of the governing equations in a standard non-dimensional form. We will consider the case of Poiseuille flow in this numerical study, but without loss of generality we can choose our characteristic length to be that of the particle R^* (the reduced radius, about 2.82μm for a RBC), the characteristic velocity to be $\dot{\gamma}_w R^*$ (the wall shear rate times the particle size), the characteristic stress in the fluid to be the $\eta_0 \dot{\gamma}_w$, the characteristic stress in the particle to be $\hat{\mu}_p / R^*$, and the timescale to be $\dot{\gamma}_w^{-1}$. This gives us the following non-dimensional equations to solve (where non-dimensional variables and operators are indicated with a star):

$$\mathrm{Re}\frac{\mathrm{D}\boldsymbol{v^*}}{\mathrm{D}t^*} = \nabla^* \cdot \boldsymbol{\sigma}^{f*} = -p^* + \nabla^* \cdot \nabla^* \boldsymbol{\lambda v^*} \quad x \in \Omega^{\mathrm{f}}, \tag{13}$$

$$\mathrm{Re}\frac{\mathrm{D}\boldsymbol{v^*}}{\mathrm{D}t^*} = \frac{1}{\mathrm{Ca}} \nabla^* \cdot \boldsymbol{\sigma}^{\mathrm{m}*} \quad x \in \Omega^{\mathrm{m}}, \tag{14}$$

$$\nabla^* \cdot \boldsymbol{v^*} = 0 \quad x \in \Omega. \tag{15}$$

We note that the viscosity may not be constant everywhere in the simulation. There are actually two different zero shear viscosities inside and outside the membrane which we will call: η_{in} and $\eta_{\mathrm{out}} = \eta_0$. Additionally, non-dimensional relationships for the energy areal density are as follows for the Skalak Model and the bending energy:

$$\hat{W}^* = \frac{1}{2}\left(\frac{1}{2}I_1^2 + I_1 - I_2\right) + \frac{\hat{\mu}_D}{8\hat{\mu}_p} I_2^2, \tag{16}$$

$$\hat{W}_B^* = \frac{\hat{\kappa}_b}{2}\left(2\kappa_H^* + c_0^*\right)^2. \tag{17}$$

This leaves us with a total of 6 dimensionless parameters: The Reynolds number ($\mathrm{Re} = \frac{\rho \dot{\gamma}_w R^{*2}}{\eta_0}$), the capsule viscosity ratio ($\lambda = \frac{\eta_{\mathrm{in}}}{\eta_{\mathrm{out}}} = \frac{\eta_{\mathrm{in}}}{\eta_0}$), and the capillary number ($\mathrm{Ca} = \frac{\dot{\gamma}_w \eta_0}{R^* \mu_p}$) appear in the evolution equations. Additionally, two ratios appear in the constitutive equations for the solids: $\frac{\hat{\mu}_D}{\hat{\mu}_p}$ and $\hat{\kappa}_b = \frac{k_b}{R^* \hat{\mu}_p}$.

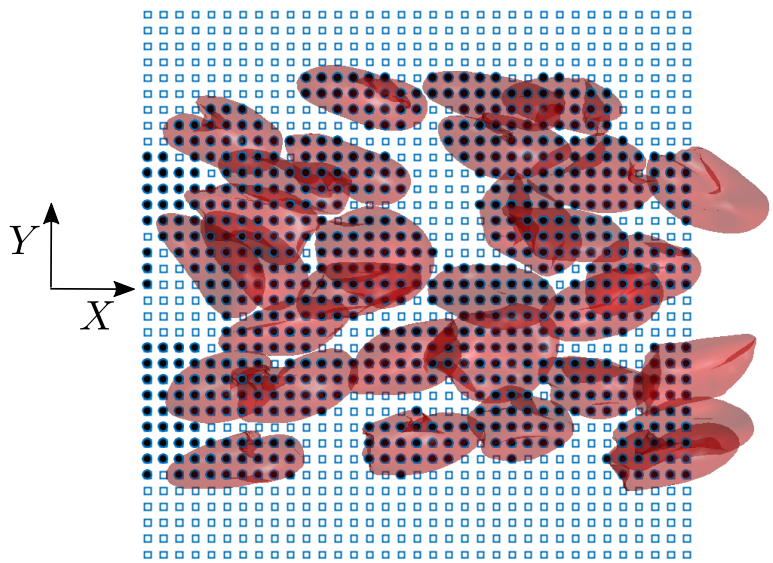

Figure 1: A graphical representation of how the distribution function is calculated. Points in filled circles are inside the RBCs at this timestep and points marked as open squares are outside (the points represent a discrete sampling of our indicator function, I). The integration at each slice in y gives a more accurate picture of the distribution than the common formation of a histogram from the center of mass locations.

For the studies presented in this paper the Reynolds number will be smaller than 10^{-1}, and the capillary number will be set to a value of 1 for all simulations. Since we desire a simulation of RBCs using the Skalak model and these systems are largely surface incompressible we will set the dimensionless ratio $\frac{\hat{\mu}_D}{\hat{\mu}_p} = 100$. The bending parameter, $\hat{\kappa}_b$, is generally much smaller than 1 (Zhao et al., 2012; Sinha and Graham, 2015) and we set it to be 0.03 for all of the simulations. The last dimensionless parameter is a geometric parameter which is the confinement ratio of our channel, $\varepsilon = \frac{R^*}{H}$. Our main aim in this manuscript is to discuss the effects that varying viscosity ratio, $\lambda = \frac{\eta_{\text{in}}}{\eta_{\text{out}}}$ has on the cell dynamics of single and multiparticle red blood cell suspensions. Additionally we will consider the effect of using two distinct channel heights (two values of $\varepsilon = \frac{1}{7}, \ \frac{1}{12}$).

Calculation of Cell Distributions and CFL

The cell distributions will be presented throughout the discussion and we desire to calculate a metric that describes concentration of red blood cells at a given position without having to resort to discrete measures. To calculate the cell distribution function, the following integral is calculated over the domain using the indicator function I and the size of the box considered (L_x, L_z):

$$\phi(y) = \frac{1}{L_x L_z} \int \int I(x, y, z) dx dz \tag{18}$$

This has been graphically illustrated in Fig. 1 where points that are inside the RBCs have been illustrated in closed circles and the points outside the RBCs have been illustrated with open squares. Oftentimes, a discrete measure of the distribution is presented which typically is a histogram of the center of masses (Qi, 2017; Zhao et al., 2012). Utilizing a histogram has the unfortunate requirement of selecting a bin size, and the selected bin size can often qualitatively change how these functions look. This integrated method produces a unique distribution function for a given RBC state that requires no parameter selection.

Additionally, we calculate the Cell Free Layer (CFL) thickness for a given RBC state by measuring the distance to the nearest red blood cell from the wall at every x plane and averaging this over the entire

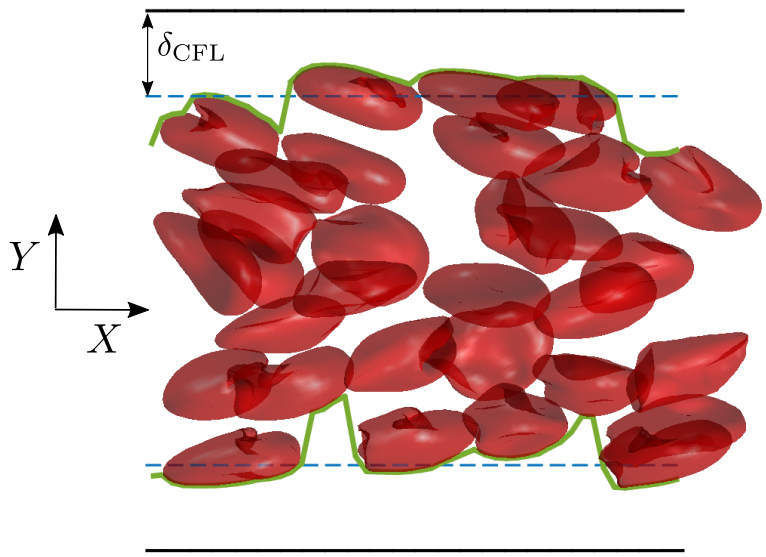

Figure 2: A graphical representation of how the CFL is calculated. The blue dashed line is the CFL thickness as calculated from the average distance a cell is away from the wall at every x-plane. These distances are plotted as a function of x as green solid lines.

domain. This has been illustrated graphically in Fig. 2 where the blue dashed line represents the calculated CFL thickness. The solid green line is the smallest distance from the wall a red blood cell is located in each x-plane as a function of x. The CFL is calculated as the average distance along this line. To calculate the CFL as a function of time, we use a running average where each data point represents the average in the domain between the two neighboring data points.

Results and Discussion

Single Cell and Binary Collision Behavior

We first consider the effect that the viscosity ratio (λ) has on the dynamics of single cells or of pairs of cells. Often for reasons of computational costs the viscosity ratio is assumed to be 1, but a realistic RBC has a viscosity ratio much closer to 5. In the following section we consider how the viscosity ratio effects the hydrodynamic lift of cells and also how the binary collision is effected by the viscosity ratio. Both of these features are key since the binary collision and lift are the two main driving forces that cause cells to migrate away from the centerline and towards the centerline respectively in many body systems. These two simple simulations can then be used as inputs into a coarse grained model such as those developed by Qi and Shaqfeh (2017).

Hydrodynamic Lift of Single Cells

We begin by considering the behavior of single cells lifting in a channel flow for two different value of viscosity ratios. The geometry utilized for this experiment is $(32 \times 7.092 \times 9)R^*$ where in x and z directions, we imposed periodic boundary condition. The Ca number for these simulations is set to 1 (very close to the physiological value in micro-capillaries). Presented in Fig. 3 we see the trajectory of two cells with a viscosity ratio of 1 and 5 plotted as a function of dimensionless time ($t^* = t\dot{\gamma}_w$). The higher viscosity ratio of 5 is plotted as diamonds and we see that compared to the lower viscosity ratio of 1 that the lift is substantially reduced.

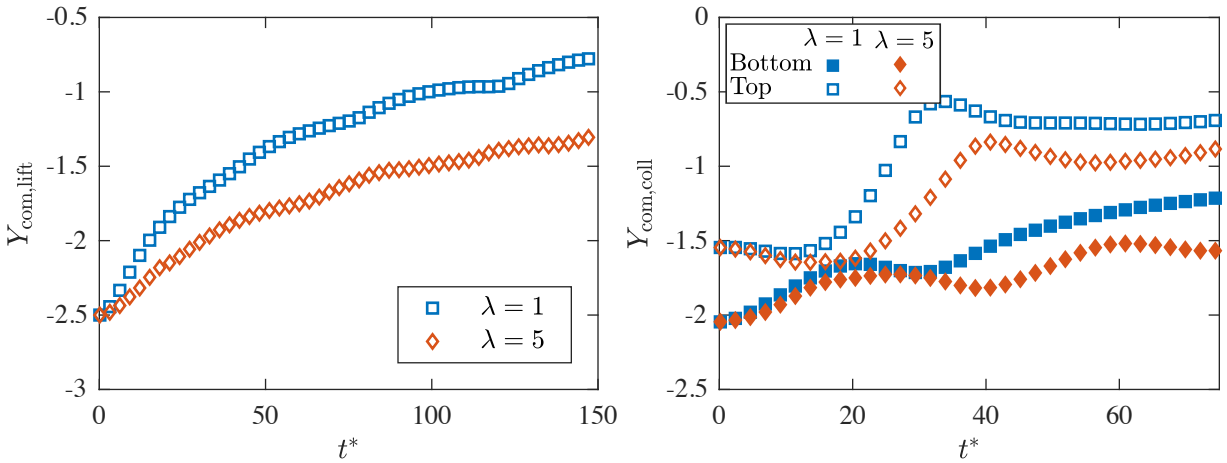

Figure 3: We plot the cell trajectory as a function of time for two cells that begin close to the wall at two viscosity ratios of 1 and 5 in the left panel. The wall is located at $Y = -3$ and the time is made dimensionless with the inverse shear rate at the wall. We see that the lift of a cell at a higher viscosity ratio of 5 (diamonds) is substantially lower than that of the cell with a viscosity ratio of 1 (squares). In the right panel we plot the trajectory of two cells undergoing a binary collisions for the same viscosity ratios of 1 and 5 (squares and diamonds). The binary collision is somewhat less effected by the viscosity ratio than the lift.

This result has considerable consequences for multiparticle systems since one of the primary driving forces for RBCs to migrate toward the center of the channel is the lift (Qi and Shaqfeh, 2017). The platelets are then squeezed to the perimeter by binary diffusion which leads ultimately to platelet margination and the formation of a Cell Free Layer (CFL). This result suggests that there is a smaller driving force to generate the cell free layer, since hydrodynamic lift at higher viscosity ratios is reduced.

Binary Cell Diffusion

Next we consider the binary collision problem in the channel flow. We again utilize a similar geometry with dimensions of $(32 \times 7.092 \times 9)R^*$ wherein the x and z directions are periodic. The Ca number in this problem is fixed to 1.69. The cells are initially started at fixed $Y_{\text{com}} = \frac{y}{R^*}$ positions of -1.5 and -2 and then allowed to collide. In Fig. 3 on the right panel we see the trajectories from this collision for both cells at two different viscosity ratios of 1 (squares) and 5 (diamonds). We see that there are differences in collision trajectory but they are less pronounced than the lift differences in the left panel of the same figure.

However, the cells that collide with one another are also constantly lifting as well. We would like to remove this factor from our analysis. In Fig. 4 on the left panel we present the same data as in Fig. 3 but with the lift trajectories subtracted from the binary collision. Now we see that the final effect of the binary collision has very little dependence on the viscosity ratio. The trajectories for the viscosity ratio of 5 (diamonds) and of 1(squares) have almost the same net displacement. This implies that the binary diffusivity for both of these systems is virtually the same. Since the lift is markedly different this allows us to conclude that the driving force for motion towards the centerline is weaker for viscosity ratio 5, but the driving force for motion away from the center is about the same (since this is binary diffusion driven). In multiparticle simulations we therefore expect the CFL to be smaller for the viscosity ratio 5 systems.

Additionally, in Fig. 4 in the right panel we have presented timelapses images of these two collisions. We note that for the lower viscosity ratio simulations the cells are initially tank treading (the top set of presented images). The higher viscosity ratio collision involves cells that are tumbling instead of tank treading. This likely explains the subtle differences in the collision trajectories presented in the left side of Fig. 4. Ultimately these simple behaviors presented here, lift and binary collision, can be used to construct

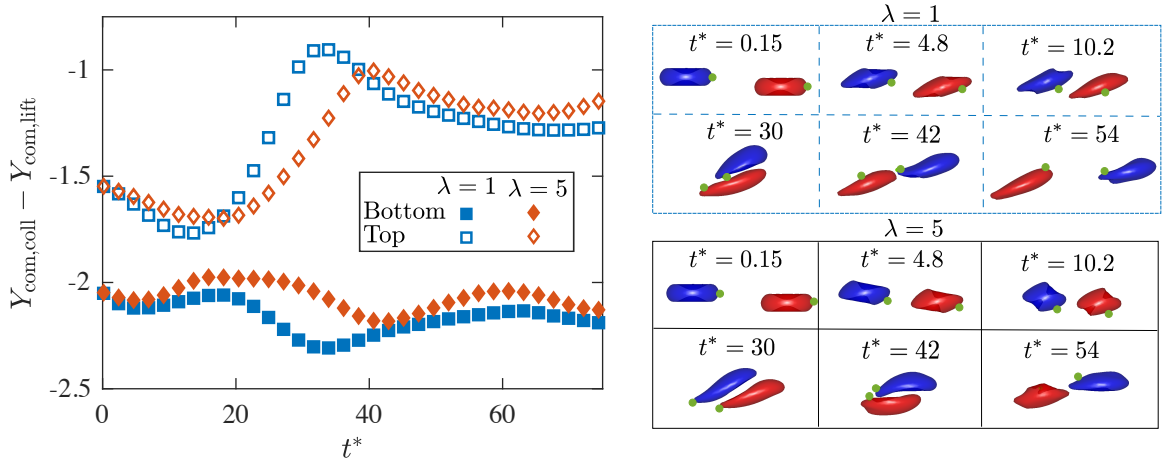

Figure 4: Presented in the left panel is the collision trajectory at two different viscosity ratios of 1 (squares) and 5 (diamonds) from Fig. 3 after subtracting of the lift contributions as a function of dimensionless time ($t^* = \dot{\gamma}_w t$). We see that after taking into account the different amount of lift that the two viscosity ratios experience that the collision trajectories have similar final displacements (therefore we expect similar binary diffusions for the different viscosity ratios). In the right panel are time lapses of these two collision processes taking place. The upper part of this panel is at a viscosity ratio of 1 and the lower one is at a viscosity ratio of 5. We note that the higher viscosity ratio exhibits more tumbling motion than the lower viscosity ratio.

a collision model. But, we alternatively, would like to examine the effects for fully resolved simulations of many red blood cells in different geometries.

RBC Suspensions with 10-20% Ht

In this section we discuss particle resolved simulations of suspensions of RBCs considering three main parameters of interest. First we will consider the effect of the channel size (ε) on the distribution of cells and the dynamics of these distributions. Then we will discuss the effect of viscosity ratio (λ) and volume fraction (also known as hematocrit for RBCs which we denote as Ht) on the distribution of cells, the CFL, as well as the observed cell shapes in these flows. The simulation of the CFL layer size in particular is of great interest at viscosity ratios greater than 1 since to date this has not been studied for small arterioles at physiological hematocrits in such simulations (and often times it is assumed that a viscosity ratio of unity is sufficient for such calculations).

RBC Distributions as a function of Channel Size

We consider the effect of channel size at fixed viscosity ratio of 1 and volume fraction of 10% on the distribution of cells in a pressure driven channel flow. Presented in Fig. 5 are the concentration profiles at a series of times for two different sized channels (on the left $\varepsilon = \frac{1}{12}$ and on the right $\varepsilon = \frac{1}{7}$). A series of dimensionless times ($\dot{\gamma}_w t$) in the range of 1 to 1000 are presented as lines of increasing thickness in these plots. One important feature to note is that for both systems we see fluctuations in the distribution that occur over very long times and these fluctuations persist even after 500 dimensionless times. Previous studies often implicitly assume that times shorter than the time of the presented distribution are sufficient to reach a steady state (de Haan et al., 2018; Shen et al., 2016; Qi, 2017), but it appears that no such steady state exists and that there is a constant state of fluctuation. Therefore, a time sequence of concentration profile is used here to interpret the results.

The other very obvious feature from Fig. 5 is that the smaller channel ($\varepsilon = \frac{1}{7}$) on the right only shows one or two maxima depending on the time and the distribution appears to fluctuate between these different

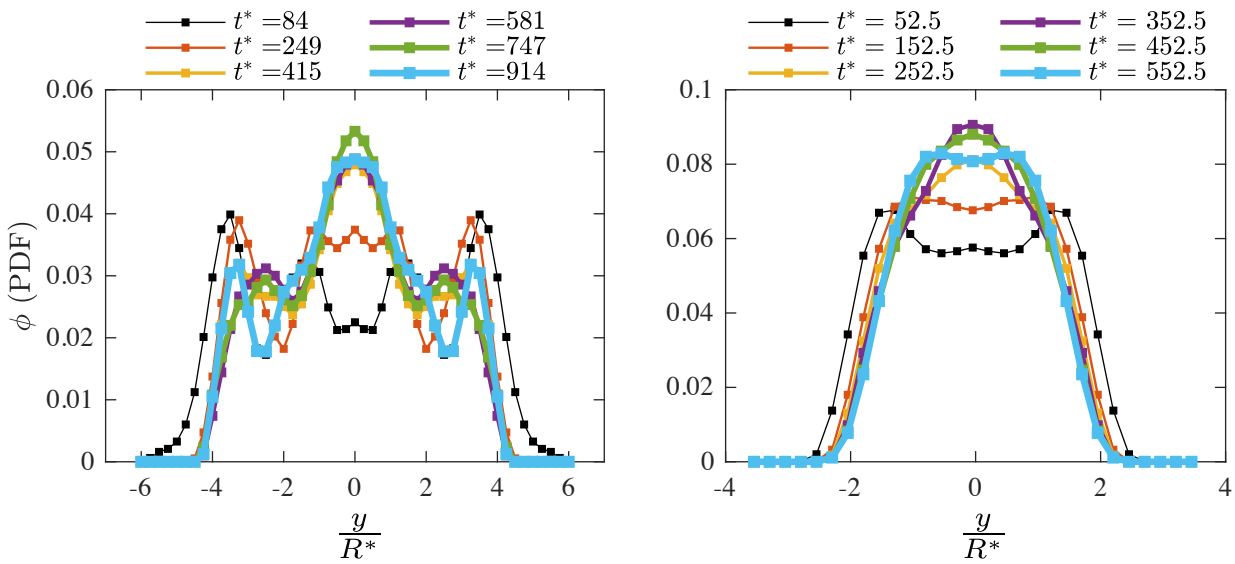

Figure 5: Concentration distribution in a pressure driven channel flow for Ca = 1. The domain is periodic in X and Z directions. The dimensionless channel dimensions are $32 \times 7 \times 9$ on the left and $20 \times 12 \times 9$ on the right where the length is non-dimensionalized with the effective radius of an RBC, R^*, which is 2.82μm.

states. This is very different from the results displayed in the left panel where there are two secondary peaks near the boundary of the CFL. These secondary peaks also seem to display similar fluctuations in size and position when compared to the bimodal distribution seen in the smaller channel. This fluctuating bimodality of the smaller channel is very interesting to observe since smaller channels have never been studied in this context despite their physiological relevance. This feature in the cell distribution undoubtedly has implications in how cells split and marginate in junctions with varying inlet sizes which is likely critical in physiological conditions.

Transient Shapes as a Function of Viscosity Ratio

We next present the effects of viscosity ratio on suspensions of RBCs at different hematocrit levels. For smaller vessel sizes the hematocrit is lower compared to the overall hematocrit and under physiological conditions. It is known that small vessels tend to have hematocrits around 10% (Fung, 1997). The first thing we consider is how the shapes of these cells differ in the two situations. It has been observed experimentally and through simulations by Lanotte et al. (2016) that there are a series of unusual shapes exhibited by cells with a viscosity ratio of 5 (the physiological viscosity ratio). These interesting shapes include tri-lobe and multi-lobe shapes. In Fig. 6 we present snapshots of a series of shapes for different red blood cells at two viscosity ratios of 1 and 5. These cells are from a suspension simulation in a pressure driven flow with $\varepsilon = \frac{1}{7}$, Ht = 10, and at Ca = 1.

In Fig. 6 in the upper panel we see two red blood cells that are observed over many dimensionless times ($\dot{\gamma}_w t$). It is clear that these cells take on relatively smooth shapes such as "slippers" and are largely tank treading at this Ca number. In the lower panel we have selected three cells from a viscosity ratio 5 suspension and we observe qualitatively different cell shapes. These shapes can all be described as multi-lobe shapes such as those observed by Lanotte et al. (2016). It is clear that the viscosity ratio of 5 is required to see such shapes in our simulated system. Another clear feature is that all of these cells largely tumble.

These shapes at larger viscosity ratios that exhibit tumbling dynamics are likely important when considering the lift dynamics of individual cells. As we saw in Fig. 3, tumbling cells at the higher viscosity lift more slowly than the tank-treading lower viscosity ratio counterparts. The shape of a cell and its mode of motion strongly influence the lift of a given cell which means we expect suspensions of these cells to have

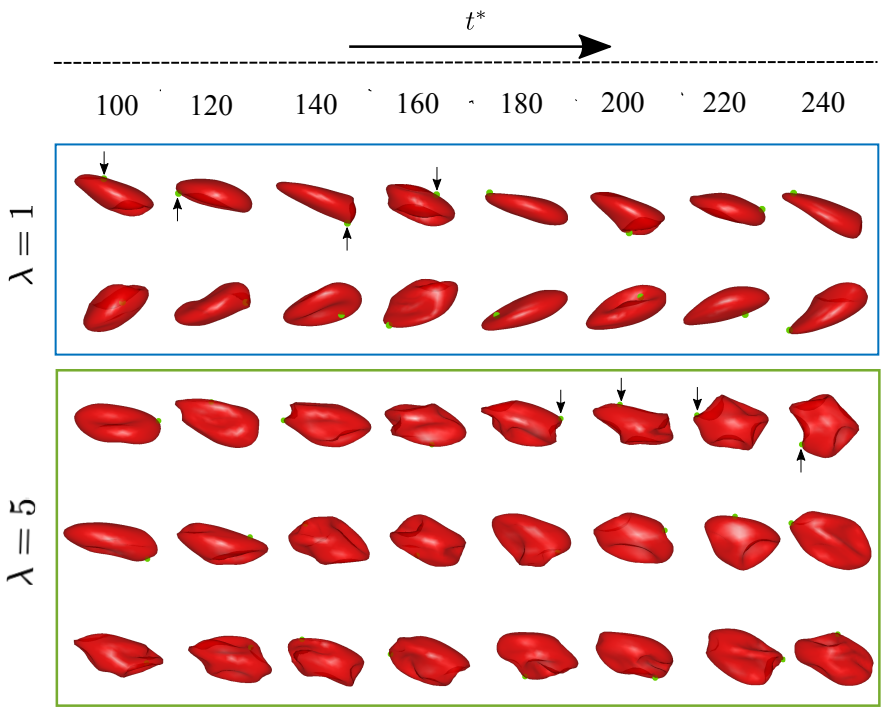

Figure 6: The shapes as a function of time for 5 cells are presented here from simulations with a volume fraction of 10% and and channel constriction of $\varepsilon = \frac{1}{7}$. The first two rows of cell images are taken from a simulation at $\lambda = 1$ and we see generally smooth shapes that tank tread. The lower three rows are from simulations at $\lambda = 5$ and we see complex multi-lobe shapes with tumbling dynamics.

different cell free layer (CFL) thicknesses and dynamics.

RBC Distributions as a Function of Hematocrit and Viscosity Ratio

Next, we consider how the distributions of cells are effected by the viscosity ratio in pressure driven flow. For this section we will only consider channels with confinement ratios $\varepsilon = \frac{1}{7}$. In addition we will consider the effects of cell volume fraction Ht = 10% or 20%. Given results demonstrated for single particles and binary collision we know the fundamental driving force of lift is different between these two viscosity ratios but the binary diffusion induced by collision is largely constant. We therefore expect that the CFL and the dynamics that lead to a steady state to be somewhat different in these cells suspensions.

In Fig. 7 we see the concentration distributions at fixed confinement of $\varepsilon = \frac{1}{7}$ for two different viscosity ratios of 1 and 5 (on the left and right respectively) for Ht = 10%. In these plots we see the main effect that we predicted from the single and double cell dynamics. The cell free layer has been reduced in size due to the lowered lift driving force. You can observe this reduced cell free layer by noting the depleted region near the two walls on the far left and right of each distribution. The distribution at higher viscosity ratio has also become substantially more blunt for viscosity ratio of 5. However, both of these systems still show substantial fluctuations in their concentration distribution as a function of time.

In Fig. 8 we consider the same comparison but at a much higher volume fraction of Ht = 20% This set of simulations were also conducted at Ca = 1 and a confinement of $\varepsilon = \frac{1}{7}$. The features presented in the set of simulations are quite different. At the higher volume fraction of 20% the distributions appear to be very similar. Even at this small channel size we see small peaks near the CFL layer (previously we only saw these in larger channel simulations) and we still see the fluctuations that we observed previously. However, now the CFL layer is nearly identical on the left and right. At high concentrations the cell free layer appears to be controlled by the finite volume the cells can occupy instead of the lift and binary collision factors that were previously much more important in lower volume fraction simulations.

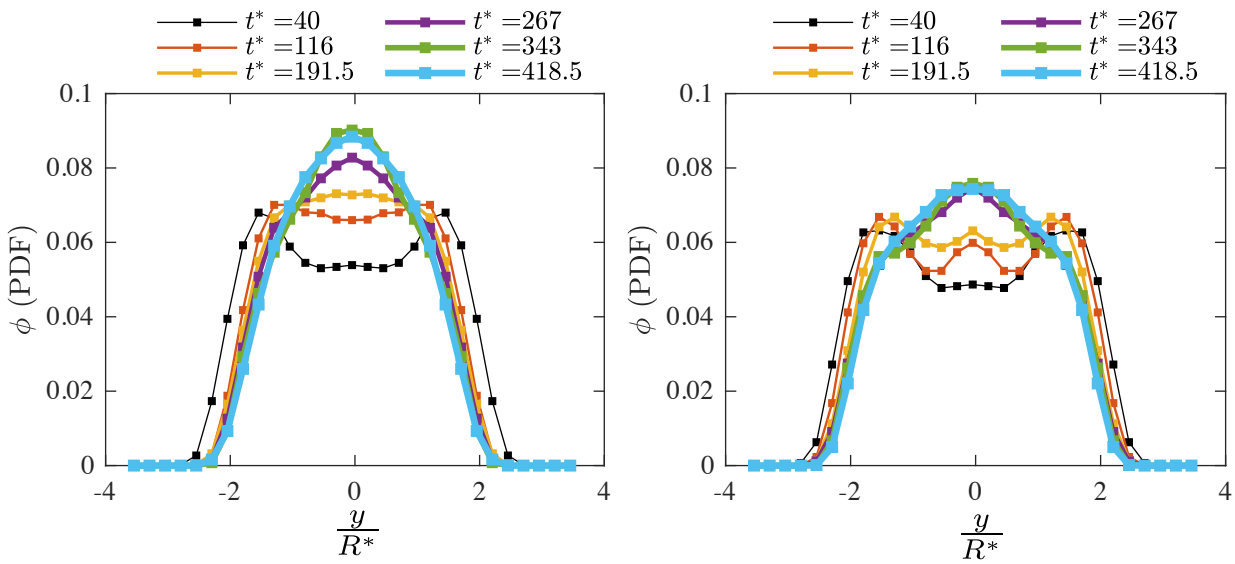

Figure 7: Concentration distribution in a pressure driven channel flow. The left is a viscosity ratio of 1 and the right is a viscosity of 5. Both panels are at a Ht = 10%, Ca = 1, and $\varepsilon = \frac{1}{7}$.

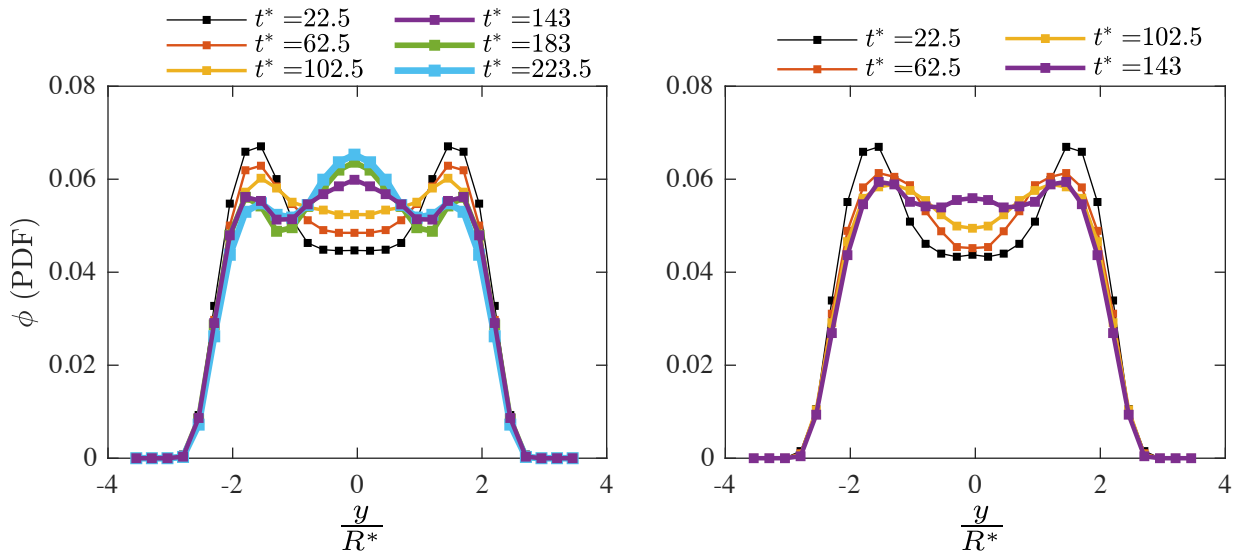

Figure 8: Concentration distribution in a pressure driven channel flow. The left is a viscosity ratio of 1 and the right is a viscosity of 5. Both panels are at a Ht = 20%, Ca=1, and $\varepsilon = \frac{1}{7}$.

We can go one step further and quantify the CFL layer for these simulations. In Fig. 9 we see the CFL plotted for the four simulations presented in Figs. 7 and 8 as a function of dimensionless time. The higher viscosity ratios of 5 are plotted as diamonds and the lower viscosity ratios of 1 are plotted as squares. Unsurprisingly, at the higher volume fraction the CFL is much smaller (due to the excluded volume and much higher cell load). And we see that the observation we made about the CFL in Fig. 8 holds true quantitatively: the CFL is virtually independent of viscosity ratio at the higher volume fraction of 20%.

When examining the lower volume fraction results we see that the CFL is strongly influenced by the viscosity ratio. The lowered capacity for lift at the higher viscosity ratio and the nearly constant binary diffusion demonstrated earlier in the single and double particle section lead to this expected result. Additionally, plotted in this figure is the steady, collision model results from Qi and Shaqfeh (2017) as dashed lines. We see good agreement between the low viscosity ratio results and the course grained theory. However, it is clear that the effects of lift and binary diffusion cause the results to deviate at high λ and low

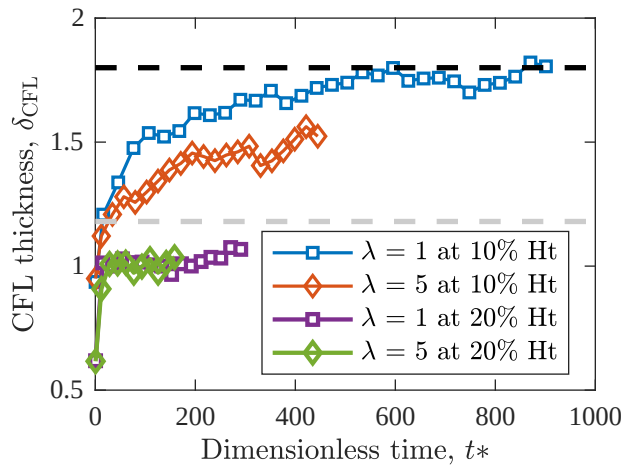

Figure 9: CFL as a function of Ht and λ and time. Additioanlly the reduced order model results form Qi et al. in 2017 are plotted in dashed lines for $\lambda = 1$. Note that the CFL is nearly invariant to viscosity ratio for higher volume fraction of 20%. The lower volume fraction of 10% shows good agreement compared to the reduced order model for low viscosity ratio, but the high viscosity ratio deviates significantly from the low λ results.

Ht.

RBC Distributions as a Function of Viscosity Ratio and Channel Size

The last feature we explore is how channel size effects CFL layer size and cell distribution for larger channel sizes with a constriction of ($\varepsilon = \frac{1}{12}$). The simulations here are conducted at a Ht = 10% and we will consider viscosity ratios of 1 and 5. In Fig. 10 the cell distributions for viscosity ratio of 1 and 5 have been presented on the left and the right respectively. We see similar trends as those seen at the higher confinement earlier in Fig. 7. CFL is smaller for the higher viscosity simulations and the bulk profile has become substantially more blunted.

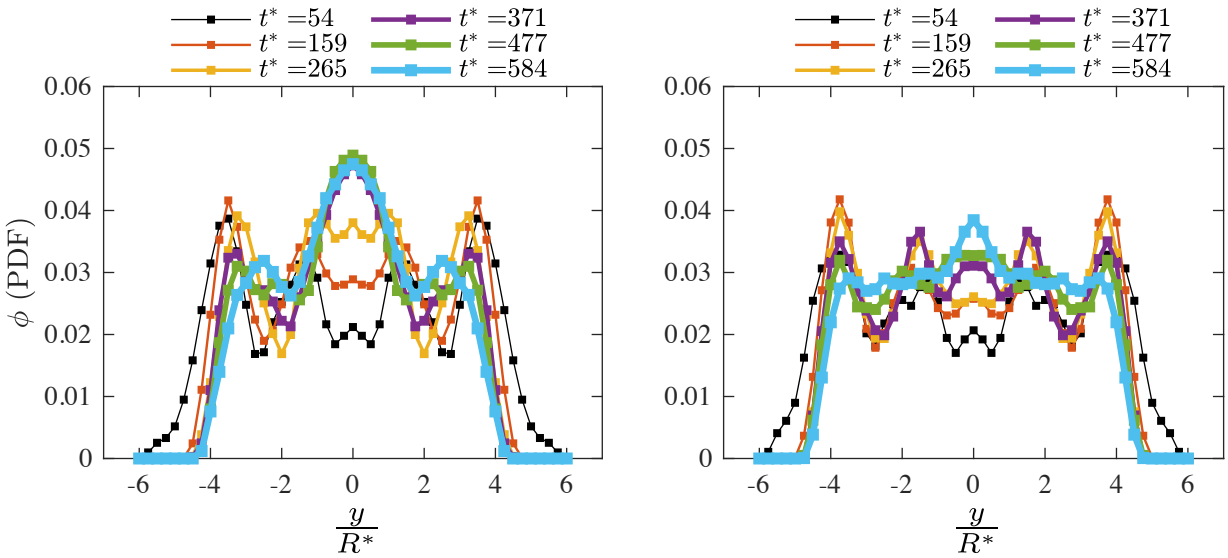

Figure 10: Concentration distribution in a pressure driven channel flow. The domain is periodic in X and Z directions. The results here are for viscosity ratios of 1 and 5 (left and right respectively). All results here are for channel heights of $12R^*$, Ca=1, and Ht = 10%.

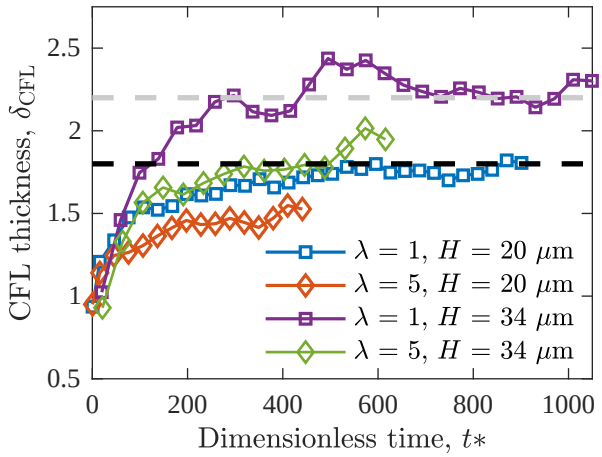

Figure 11: CFL as a function of ε and λ and time. Additionally the reduced order model results form Qi et al. in 2017 are plotted in dashed lines for $\lambda = 1$. The results show good agreement compared to the reduced order models for low viscosity ratio, but the high viscosity ratio deviates significantly from the low λ results.

We can again quantify the CFL from these simulations and compare against the more confined simulations. In Fig. 11 we see the CFL plotted as a function of time for the simulations presented in Figs. 7 and 10. Again the steady results from the collision theory by Qi (2017) are presented as dashed lines. Similar reductions in the CFL size are seen as λ is increased in these simulations that are both at Ht = 10% and we again see good agreement between the collision model and the steady state CFL for both channel sizes if $\lambda = 1$. This allows us to conclude that the results of CFL reduction are largely generic and only a function of the volume fraction, Ht, and the viscosity ratio, λ.

Conclusions

In this study we consider the effect of volume fraction (Ht), viscosity ratio (λ), and confinement (ε) on cell suspension dynamics. We consider values of hematocrit of 1 and 5 where the latter is more physiologically relevant but the former is utilized considerably in theoretical calculations for simplicity. Additionally, we compare two confinement sizes that both correspond to appropriate micro-vasculature dimensions ($\varepsilon = \frac{1}{7}, \frac{1}{12}$).

The first key finding of these simulations is that channel size qualitatively effects the cell distribution. Smaller channels produce distributions that fluctuate between a bi-modal and single mode distribution and these oscillations persist for long times. On the other hand less confined simulations show three peaks with one large center peak and two secondary peaks near the walls. These peaks also fluctuate and as far as we can tell do not reach a steady state. The lack of steady-state for these simulations and the difference in distributions is something that has not been previously reported in the literature.

In addition, we see that CFL and cell distributions change dramatically when the volume fraction considered is low (Ht = 10%) for all channel sizes. This volume fraction is physiologically relevant for small arterioles. The CFL is reduced in size and the major peaks in the core of the distribution are blunted. We demonstrate for single cells that increasing the viscosity ratio decreases lift but does little to the binary diffusion induce by collision. The weakened driving force towards the center of the channel from lift with the unchanged diffusive contribution likely leads to a reduced CFL size. This result has important implications for simulations of hemostasis in small arterioles since the change in CFL impacts the available space for platelets in physiological conditions.

Lastly, we find that at higher volume fractions (Ht = 20%) that there are very few changes to the cell distribution and the CFL when the viscosity ratio is changed. In these situations (which are slightly above the physiological hematocrit for arterioles of the size that we are simulating (Fung, 1997; Shen et al., 2016)) the excluded volume effects from the large number of cells seem to dominate the behavior leading to small, similarly sized CFL layers in both cases.

The tool and methodology employed herein can be used to study complex geometries that are not simple straight channels. We plan to further use these tools to asses the effects of complex channel geometry on the CFL and cell dynamics at physiological viscosity ratios.

Author Contributions

A. Saadat and C.J. Guido designed the research, carried out all simulations, analyzed the data, and wrote the article.

Acknowledgments

The authors of this paper would like to acknowledge support from NSF (CBET-1803765), the US Army High Performance Computation Research Center (AHPCRC) with the grant number W911NF07200271, and the Open Medicine Foundation (OMF). Computer simulations were performed on AHPCRC's Excalibur cluster, the Stanford University Certainty cluster, and XSEDE's COMET cluster.

Conflicts of Interest

There are no conflicts of interest to report.

References

Bächer, C., Kihm, A., Schrack, L., Kaestner, L., Laschke, M. W., Wagner, C., and Gekle, S. (2018). Antimargination of microparticles and platelets in the vicinity of branching vessels. *Biophysical journal*, 115(2):411–425.

Bagchi, P. and Kalluri, R. M. (2009). Dynamics of nonspherical capsules in shear flow. *Phys. Rev. E*, 80:016307.

Balogh, P. and Bagchi, P. (2018). Analysis of red blood cell partitioning at bifurcations in simulated microvascular networks. *Physics of Fluids*, 30(5):051902.

Coupier, G., Kaoui, B., Podgorski, T., and Misbah, C. (2008). Noninertial lateral migration of vesicles in bounded poiseuille flow. *Physics of Fluids*, 20(11):111702.

Danker, G., Vlahovska, P. M., and Misbah, C. (2009). Vesicles in poiseuille flow. *Phys. Rev. Lett.*, 102:148102.

de Haan, M., Zavodszky, G., Azizi, V., and Hoekstra, A. (2018). Numerical investigation of the effects of red blood cell cytoplasmic viscosity contrasts on single cell and bulk transport behaviour. *Applied Sciences*, 8(9):1616.

Doddi, S. (2008). *Three-dimensional Computational Modeling and Simulation of Biological Cells and Capsules*. PhD thesis, Rutgers.

Eggleton, C. D. and Popel, A. S. (1998). Large deformation of red blood cell ghosts in a simple shear flow. *Physics of Fluids*, 10(8):1834–1845.

Evans, E. and Fung, Y.-C. (1972). Improved measurements of the erythrocyte geometry. *Microvascular Research*, 4(4):335 – 347.

Fedosov, D. A., Caswell, B., Popel, A. S., and Karniadakis, G. E. (2010). Blood flow and cell-free layer in microvessels. *Microcirculation*, 17:615–628.

Fedosov, D. A., Peltomaki, M., and Gompper, G. (2014). Deformation and dynamics of red blood cells in flow through cylindrical microchannels. *Soft Matter*, 10:4258–4267.

Fischer, T. M., Haest, C. W., Stöhr-Liesen, M., Schmid-Schönbein, H., and Skalak, R. (1981). The stress-free shape of the red blood cell membrane. *Biophys J.*, 34(3):409?422.

Fitzgibbon, S., Cowman, J., Ricco, A. J., Kenny, D., and Shaqfeh, E. S. G. (2015). Examining platelet adhesion via stokes flow simulations and microfluidic experiments. *Soft Matter*, 11:355–367.

Foessel, E., Walter, J., Salsac, A.-V., and Barthés-Biesel, D. (2011). Influence of internal viscosity on the large deformation and buckling of a spherical capsule in a simple shear flow. *J. Fluid Mech.*, 672:477–486.

Freund, J. B. (2014). Numerical simulation of flowing blood cells. *Annual review of fluid mechanics*, 46:67–95.

Freund, J. B. and Orescanin, M. (2011). Cellular flow in a small blood vessel. *Journal of Fluid Mechanics*, 671:466–490.

Fung, Y. (1997). *Biomechanics: Circulation*. Springer.

Fåhræus, R. and Lindqvist, T. (1931). The viscosity of the blood in narrow capillary tubes. *American Journal of Physiology-Legacy Content*, 96(3):562–568.

Govindarajan, V., Rakesh, V., Reifman, J., and Mitrophanov, A. (2016). Computational study of thrombus formation and clotting factor effects under venous flow conditions. *Biophysical Journal*, 110(8):1869 – 1885.

Guckenberger, A., Kihm, A., John, T., Wagner, C., and Gekle, S. (2018). Numerical-experimental observation of shape bistability of red blood cells flowing in a microchannel. *Soft Matter*, 14:2032–2043.

Haga, J. H., Beaudoin, A. J., White, J. G., and Strony, J. (1998). Quantification of the passive mechanical properties of the resting platelet. *Annals of biomedical engineering*, 26(2):268–277.

Ham, F., Mattsson, K., and Iaccarino, G. (2006). Accurate and stable finite volume operators for unstructured flow solvers. *Annual Research Briefs*, pages 243–261.

Kaoui, B., Biros, G., and Misbah, C. (2009). Why do red blood cells have asymmetric shapes even in a symmetric flow? *Phys. Rev. Lett.*, 103:188101.

Krüger, T. (2012). *Computer Simulation Study of Collective Phenomena in Dense Suspensions of Red Blood Cells under Shear*. Springer.

Lanotte, L., Mauer, J., Mendez, S., Fedosov, D. A., Fromental, J.-M., Claveria, V., Nicoud, F., Gompper, G., and Abkarian, M. (2016). Red cells's dynamic morphologies govern blood shear thinning under microcirculatory flow conditions. *Proceedings of the National Academy of Sciences*, 113(47):13289–13294.

Mendez, S., Gibaud, E., and Nicoud, F. (2014). An unstructured solver for simulations of deformable particles in flows at arbitrary reynolds numbers. *Journal of Computational Physics*, 256:465 – 483.

Mitrophanov, A. Y., Wolberg, A. S., and Reifman, J. (2014). Kinetic model facilitates analysis of fibrin generation and its modulation by clotting factors: implications for hemostasis-enhancing therapies. *Mol. BioSyst.*, 10:2347–2357.

Narsimhan, V., Zhao, H., and Shaqfeh, E. S. G. (2013). Coarse-grained theory to predict the concentration distribution of red blood cells in wall-bounded couette flow at zero reynolds number. *Physics of Fluids*, 25(6):061901.

Omori, T., Ishikawa, T., Imai, Y., and Yamaguchi, T. (2013). Shear-induced diffusion of red blood cells in a semi-dilute suspension. *J. Fluid Mech.*, 724:154–174.

Omori, T., Ishikawa, T., Imai, Y., and Yamaguchi, T. (2014). Hydrodynamic interaction between two red blood cells in simple shear flow: its impact on the rheology of a semi-dilute suspension. *Computational Mechanics*, 54(4):933–941.

Pozrikidis, C. (1992). *Boundary Integral and Singularity Methods for Linearized Viscous Flow.* Cambridge Texts in Applied Mathematics. Cambridge University Press.

Pozrikidis, C. (2003). Numerical simulation of the flow-induced deformation of red blood cells. *Annals of Biomedical Engineering*, 31(10):1194–1205.

Pranay, P., Henríquez-Rivera, R. G., and Graham, M. D. (2012). Depletion layer formation in suspensions of elastic capsules in newtonian and viscoelastic fluids. *Physics of Fluids*, 24(6):061902.

Pries, A. and Secomb, T. (2003). Rheology of the microcirculation. *Clinical Hemorheology and Microcirculation.*

Qi, Q. (2017). *Understanding Particle Migration, Margination and Adhesion in Cellular Suspensions.* PhD thesis, Stanford University.

Qi, Q. M. and Shaqfeh, E. S. G. (2017). Theory to predict particle migration and margination in the pressure-driven channel flow of blood. *Phys. Rev. Fluids*, 2:093102.

Qi, Q. M. and Shaqfeh, E. S. G. (2018). Time-dependent particle migration and margination in the pressure-driven channel flow of blood. *Phys. Rev. Fluids*, 3:034302.

Quint, S., Christ, A. F., Guckenberger, A., Himbert, S., Kaestner, L., Gekle, S., and Wagner, C. (2017). 3d tomography of cells in micro-channels. *Applied Physics Letters*, 111(10):103701.

Reasor, D., Clausen, J., and Aidun, C. (2013). Rheological characterization of cellular blood in shear. *Journal of Fluid Mechanics*, 726:497–516.

Reichel, F., Mauer, J., Nawaz, A. A., Gompper, G., Guck, J., and Fedosov, D. A. (2018). High-throughput microfluidic characterization of erythrocyte shape and mechanical variability. *bioRxiv.*

Saadat, A., Guido, C. J., Iaccarino, G., and Shaqfeh, E. S. G. (2018). Immersed-finite-element method for deformable particle suspensions in viscous and viscoelastic media. *Phys. Rev. E*, 98:063316.

Secomb, T. W. (2017). Blood flow in the microcirculation. *annual Review of Fluid Mechanics*, 49:443–461.

Shen, Z., Coupier, G., Kaoui, B., Polack, B., Harting, J., Misbah, C., and Podgorski, T. (2016). Inversion of hematocrit partition at microfluidic bifurcations. *Microvascular Research*, 105:40 – 46.

Sigüenza, J., Mendez, S., Ambard, D., Dubois, F., Jourdan, F., Mozul, R., and Nicoud, F. (2016). Validation of an immersed thick boundary method for simulating fluid?structure interactions of deformable membranes. *Journal of Computational Physics*, 322:723 – 746.

Sinha, K. and Graham, M. D. (2015). Dynamics of a single red blood cell in simple shear flow. *Phys. Rev. E*, 92:042710.

Smart, J. R. and Leighton, D. T. (1991). Measurement of the drift of a droplet due to the presence of a plane. *Physics of Fluids A: Fluid Dynamics*, 3(1):21–28.

Spann, A. P., Campbell, J. E., Fitzgibbon, S. R., Rodriguez, A., Cap, A. P., Blackbourne, L. H., and Shaqfeh, E. S. (2016). The effect of hematocrit on platelet adhesion: Experiments and simulations. *Biophysical Journal*, 111(3):577 – 588.

Tomaiuolo, G., Lanotte, L., D'Apolito, R., Cassinese, A., and Guido, S. (2016). Microconfined flow behavior of red blood cells. *Medical Engineering & Physics*, 38(1):11 – 16. Micro and Nano Flows 2014 (MNF2014) - Biomedical Stream.

Vahidkhah, K. (2015). *Three-dimensional computational simulation of multiscale multiphysics cellular/particulate processes in microcirculatory blood flow.* PhD thesis, Rutgers.

Yazdani, A. Z. K. (2012). *Dynamics of erythrocytes, vesicles and capsules in shear flow: The role of membrane bending stiffness and membrane viscosity.* PhD thesis, Rutgers.

Ye, T., Li, H., and Lam, K. (2010). Modeling and simulation of microfluid effects on deformation behavior of a red blood cell in a capillary. *Microvascular Research*, 80(3):453 – 463.

Ye, T., Phan-Thien, N., and Lim, C. T. (2016). Particle-based simulations of red blood cells?a review. *Journal of biomechanics*, 49(11):2255–2266.

Závodszky, G., van Rooij, B., Azizi, V., Alowayyed, S., and Hoekstra, A. (2017). Hemocell: a high-performance microscopic cellular library. *Procedia Computer Science*, 108:159–165.

Zhao, H., Isfahani, A. H., Olson, L. N., and Freund, J. B. (2010). A spectral boundary integral method for flowing blood cells. *Journal of Computational Physics*, 229(10):3726–3744.

Zhao, H., Shaqfeh, E. S. G., and Narsimhan, V. (2012). Shear-induced particle migration and margination in a cellular suspension. *Physics of Fluids*, 24(1):011902.